128 × 128 long-wavelength/mid-wavelength two-color HgCdTe infrared focal plane array detector with ultralow spectral cross talk

Weida Hu,[1,*] Zhenhua Ye,[2,5] Lei Liao,[3] Honglei Chen,[2] Lu Chen,[2] Ruijun Ding,[2] Li He,[2] Xiaoshuang Chen,[1,4] and Wei Lu[1]

[1]*National Laboratory for Infrared Physics, Shanghai Institute of Technical Physics, Chinese Academy of Sciences, Shanghai 200083, China*

[2]*Key Laboratory of Infrared Imaging Materials and Detectors, Shanghai Institute of Technical Physics, Chinese Academy of Sciences, Shanghai 200083, China*

[3]*Department of Physics and Key Laboratory of Artificial Micro- and Nano-Structures of Ministry of Education, Wuhan University, Wuhan 430072, China*

[4]*e-mail: xschen@mail.sitp.ac.cn*

[5]*e-mail: zhye@mail.sitp.ac.cn*

**Corresponding author: wdhu@mail.sitp.ac.cn*

Received June 18, 2014; revised July 29, 2014; accepted July 29, 2014; posted July 30, 2014 (Doc. ID 214198); published August 27, 2014

High temporal and spatial coherent simultaneous long-wavelength/mid-wavelength (LW/MW) two-color focal plane array (FPA) infrared detection is the cutting-edge technique for third-generation infrared remote sensing. In this Letter, HgCdTe LW/MW two-color infrared detectors were designed and fabricated. The top long-wavelength and bottom mid-wavelength infrared planar photodiodes were processed by selective B^+-implantation after etching the long-wavelength epilayer into a curvature and exposing the mid-wavelength layers for the implantation of the n region of the MW photodiode by a micro-mesa array technique. A 128 × 128 MW/LW HgCdTe infrared FPA detector is fabricated photo-lithographically by simultaneous nonplanar B^+-implantation of the LW and MW photodiodes, passivation and metallization of the sidewalls, mesa isolation, and flip-chip hybridization with a read-out integrated circuit. The inner mechanisms for suppressing the cross talk and improving photoresponse have been carried out by combining experimental work with numerical simulations.

OCIS codes: (040.3060) Infrared; (040.5160) Photodetectors; (040.1880) Detection; (040.1240) Arrays; (110.3080) Infrared imaging.

http://dx.doi.org/10.1364/OL.39.005184

As HgCdTe photovoltaic infrared (IR) detectors can offer faster response times, higher sensitivity and/or near-room-temperature operations, multicolor detections over other infrared detectors, there has been exciting progress in the development of HgCdTe photovoltaic infrared detectors during the past few years [1–5]. More recently, driven by demands for both civilian (earth observation, environment remote sensing and monitoring) and military (target discrimination and identification, and background clutter rejection) applications [6–9], two-color (or dual-band) HgCdTe detectors are widely demonstrated and investigated. Integrated as a single pixel in a focal plane array (FPA), a two-color detector can detect two spectral bands separately and independently with high temporal and spatial coherence. It provides an additional dimension of contrast that is available for signal processing and serves as a visual aid in scene interpretation, allowing determination of both absolute temperature and unique signatures of the objects from the background, while used to acquire infrared images [10]. Detecting and identifying a military threat as well as the need to reduce size, weight, and power consumption (SWaP [11], note that it is also called SWaP3 [12] for size, weight, and "power + performance + price") of thermal sights is the main target of present infrared technology. In addition to the development of third-generation infrared modules providing high resolution (HR) Si/GaAs-based [13] and higher operation temperature (HOT) heterostructure-based [14,15] detection capability, the use of two-color detection is a competitive way to realize reduced SWaP for infrared technology development. Recently, several groups have presented interesting results on two-color/dual-band FPAs over the entire 2–12 μm wavelength region. Ballet *et al.* have reported on a sequential-mode, dual band, mid-wavelength HgCdTe infrared detector on CdZnTe and CdTe/Ge substrates with pixel arrays of 128 × 128 [16]. Smith and co-workers from Raytheon have reported on a sequential-mode, long-wavelength/mid-wavelength (LW/MW) HgCdTe IR detector using an $n - p^+ - n$ heterojunction architecture with pixel arrays of 256×256, 640×480, and 1280×720 [17,18]. More recently, a 512×512 HgCdTe FPA for bias-selectable dual-band LW/LW IR detection was reported by the same group [19]. The dark-current performance for the LW detector is approaching that of single-color, liquid-phase epitaxy (LPE) LW IR detectors. 256 × 1 and 128 × 128 FPAs of HgCdTe SW/MW IR detectors with an $n^+ - p - \mathrm{P} - \mathrm{P} - \mathrm{N}$ heterojunction architecture on GaAs substrate have been fabricated and optimized in our group [20,21]. To further improve the performance of IR detector arrays, numerical simulations have also been carried out by several groups. Jozwikowski and Rogalski [22] and Wenus *et al.* [23] investigated the theoretical performance of simultaneous dual-band LW/MW HgCdTe detectors with $\mathrm{P} - n - \mathrm{N} - \mathrm{P}$ heterostructure, showing the calculated spatial distribution of electrical potential, gain, sensitivity, noise generation, and cross talk. Bellotti and Orsogna reported on a full

three-dimensional numerical simulation of simultaneous two-color MW/LW and LW/very-long-wave (VLW) IR detectors [24]. The work shows that it is possible to predict with relatively good accuracy the performance of complex detectors by using a physics-based numerical model. Recently, electrical cross talk in two-color devices using a mesa $n-p-n$ structure has been investigated using a finite-element modeling approach by Wehner *et al.* [25]. They found that a layer design is critical to ensure minimum cross talk at small pixel pitches. As it is not enough to prevent all cross talk between pixels, physical separation by full mesa design is the only practical choice. Although there have been exciting developments for two-color IR detectors during the past few years, temporal and spatial coherent simultaneous two-color LW/MW HgCdTe IR detectors have not been well investigated and designed. Specifically, groove aperture and absorption layer design of simultaneous two-color LW/MW HgCdTe IR detectors strongly restrict quantum efficiency (QE) and cross talk.

In this Letter, we report on a highly temporal and spatially coherent, simultaneous two-color LW/MW HgCdTe photovoltaic detector from theoretical design to device fabrication. Structure designs by using numerical simulations are investigated and implemented for the subsequent fabrications. Nonplanar boron ion implantation and metallization are developed by using photoresist spray-coating technology for the two-color HgCdTe IR detector. A 128×128 pixel array is achieved after the nonplanar implantation of MW and LW diodes, sidewall passivation and metallization, and flip-chip hybridization with a readout integrated circuit.

Figure 1(a) shows the schematic of a two-color LW/MW HgCdTe photovoltaic detector with an $n_1^+ - p_1 - \mathrm{P} - p_2 - n_2^+$ architecture. Under back-illumination, the bottom $p_2 - n_2^+$ junction absorbs MW radiation for wavelengths up to its cutoff value. This p-type layer junction for MW light also acts as a transparent window for LW light to pass through and be absorbed by the horizontal $n_1^+ - p_1 - \mathrm{P} - p_2$ junction with LW cutoff, as shown in Figs. 1(b) and 1(c). There are two important parameters

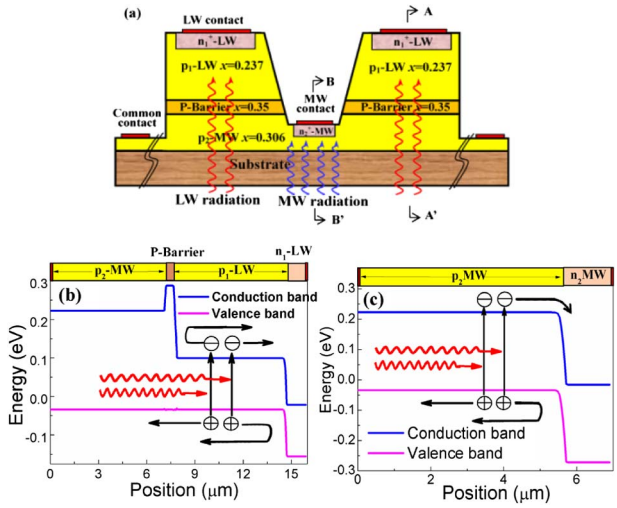

Fig. 1. (a) Schematic of grooved HgCdTe two-color infrared detector. (b) Equilibrium energy band diagram cut at A – A′. (c) Equilibrium energy band diagram cut at B – B′.

for the two-color MW/LW HgCdTe detector: (1) absorption layer thickness and (2) opening dimensions of the groove (the length of the groove top, L_{top}; the length of the groove bottom, L_{bot}). The absorption layer thickness is strongly correlated to the cross talk of MW-to-LW and LW-to-LW, as well as the QE. The opening dimension of the groove (isosceles trapezoid) is designed for simultaneous signal reading of MW junction. Additionally, the duty cycle and QE of the LW junction are strongly affected by L_{bot}.

A $p_1 - \mathrm{P} - p_2$ heterostructure HgCdTe film was first grown by molecular beam epitaxy (MBE) on (211) B oriented GaAs substrates, where P is the barrier layer with a Cd mole fraction larger than that of the p_1 and p_2 layers. Then a micro-mesa array technique is used to etch the p_1 and P layers into a curvature and expose the p_2 layers for the implantation of the n region of the MW photodiode. Note that the etching process must precisely pass though the p_1 and P layers. An over etching could possibly shorten the absorption layer thickness of the MW photodiode, and an insufficient etching of the p_1 and P layers could also fail the two-color junction design. A photoresist spray-coating technology was developed and used to open the window of nonplanar implantation and metallization/passivation of the curvature-etched sidewall. A 128×128 array detector was then fabricated photolithographically by simultaneous nonplanar B^+-implantation of the LW and MW photodiodes, passivation and metallization of the sidewalls, mesa isolation, and flip-chip hybridization with a read-out integrated circuit. The specific details of the detector are listed in Table 1.

Before discussing the design and fabrication of LW/MW HgCdTe detectors, the definition of cross talk should be clarified. Spectral cross talk in a photodetector consists of optical cross talk and electrical cross talk. The cross talk is the ratio of the photoresponse/photocurrent in either of the adjacent pixels/junction to that in the central pixel/junction [21,25]. Here, junction-to-junction cross talk is generally referring to the cross talk of two-color/multicolor detectors. In this Letter, we focus on the spectral cross talk within one pixel of LW/MW HgCdTe detector arrays, and the cross talk from pixel to pixel is not considered as the pixel pitch fabricated in this Letter is quite large [25]. Specifically, there are two kinds of cross talk for the two junctions: $C_{\mathrm{MW-to-LW}}$ (cross talk of MW-to-LW), is defined as the ratio of the signal from the MW junction to that from the LW junction under the LW radiation for the LW photodiode; $C_{\mathrm{LW-to-MW}}$ (cross talk of LW-to-MW) is defined as the ratio of the signal from the LW junction to that from the MW junction under the MW radiation for the MW photodiode. At a specific incident wavelength, the cross talk is the ratio of photoresponse/photocurrent in one junction to that in the other. For a LW/MW two-color detector, the LW-to-MW optical cross talk ($C_{\lambda \mathrm{o-LW-to-MW}}$) is generated due to the optical response to the remaining MW light in the LW absorption layer. However, little LW light can be absorbed in the MW absorption layer, so the MW-to-LW optical cross talk ($C_{\lambda \mathrm{o-MW-to-LW}} \approx 0$) from the optical response of the remaining LW light is negligible. The electrical cross talk is generated due to nonequilibrium carrier diffusion between two absorption layers. Both the electrical cross talk of LW to MW ($C_{\lambda e\mathrm{-LW-to-MW}}$)

Table 1. Material and Structural Parameters of the Two-Color HgCdTe Photodetector at 77 K

Parameters	Value of LW (Units)	Value of MW (Units)	Value of Barrier (Units)
Cd molar fraction (x)	0.232	0.309	0.35
Doping density of N region	1×10^{17}(cm^{-3})	1×10^{17}(cm^{-3})	—
Doping density of P region	8×10^{15}(cm^{-3})	8×10^{15}(cm^{-3})	8×10^{15}(cm^{-3})
Thickness of N region	1.2 (μm)	1.2 (μm)	—
Thickness of P region	9 (μm)	5–8 (μm)	0.8 (μm)

and the electrical cross talk of MW to LW ($C_{\lambda e\text{–MW–to–LW}}$) contribute to the total spectral cross talk dependent on thickness and band energy offset of the barrier layer (as shown in Fig. 1). Therefore, the total spectral cross talk is then the ratio of integral photoresponse/photocurrent in one junction to that in the other. This can be expressed as

$$C_{\text{MW–to–LW}} = \int_{\lambda} C_{\lambda e\text{–MW–to–LW}} + C_{\lambda o\text{–MW–to–LW}} = \int_{\lambda} C_{\lambda e\text{–MW–to–LW}}, \quad (1)$$

$$C_{\text{LW–to–MW}} = \int_{\lambda} C_{\lambda e\text{–LW–to–MW}} + C_{\lambda o\text{–LW–to–MW}}. \quad (2)$$

Because the LW-to-MW optical cross talk ($C_{\lambda o\text{–LW–to–MW}}$) due to the optical response of the remaining MW light in the LW absorption layer is strongly dependent on the thickness of the MW layer (p_2), the thickness of the MW layer should be optimized before device fabrication. To extract the optimal value of absorption thickness and opening dimensions of the groove, two dimensional numerical simulations using a Sentaurus Device [26] are carried out. For plain drift-diffusion simulation, the well-known Poisson equation and continuity equations are used. The carrier generation–recombination process consists of Shockley–Read–Hall, Auger, and optical generation–recombination terms. The detail simulation models (including mobility) and coefficients can be found in Refs. [9,27]. Figure 2 shows the QE and cross talk as a function of the thickness of the MW layer for the grooved $n_1^+ - p_1 - \text{P} - p_2 - n_2^+$ HgCdTe two-color infrared detector. It is found that a minimum MW-to-LW cross talk and maximum MW QE can be achieved with a MW layer of approximately 7 μm. To further optimize the groove structure, the QEs with different L_{top} and L_{bot} are calculated at cutoff wavelengths. It indicates that the MW QE at the MW cutoff wavelength of 4.8 μm increases with L_{bot} (no dependence on L_{top}). When $L_{bot} \geq 14$ μm, the MW QE saturates at a maximum value as the photogenerated carriers with the diffuse length of ~10 μm are efficiently collected by the MW contact. Figure 3 shows the QEs as functions of ($L_{top} - L_{bot}$) and L_{bot} at the cutoff wavelengths of 9.7 μm. Considering the angle of the mesa slope (within 50°–70°, namely $6.6 \leq (L_{top} - L_{bot}) \leq 15.1$, an overly large angle of mesa slope may increase the difficulty of metallization of the sidewalls) and the center-to-center spacing of the pixels, the optimal QEs for the LW and MW junctions can be achieved with $L_{top} \approx 25$ μm and $L_{bot} \approx 14$ μm from Fig. 3.

Figure 4(a) shows the designed Cd mole fraction of the p_1, P, and p_2 layers during the HgCdTe material epitaxial growth according to the simulation results. A 0.8 μm barrier layer is used to suppress the electrical cross talk. Simulations show that a barrier layer thickness larger than 500 nm can strongly suppress the electrical cross talk (less than 0.1%, not shown here). Figure 4(b) shows the scanning electron microscope (SEM) image of the fabricated detector with 128×128 pixels. Each pixel has a groove with a top diameter of 25 μm and a bottom diameter of 14 μm. The photosensitive area is 50 μm × 50 μm for each pixel. Note that the effective photosensitive area for the LW junction is less than the designed

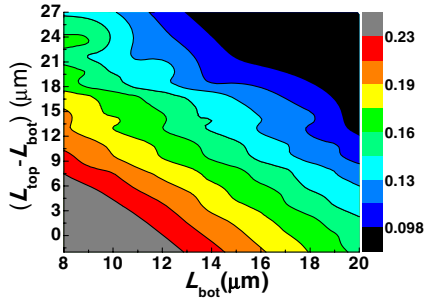

Fig. 3. LW QE as functions of ($L_{top} - L_{bot}$) and L_{bot} at a LW cutoff wavelength of 9.7 μm.

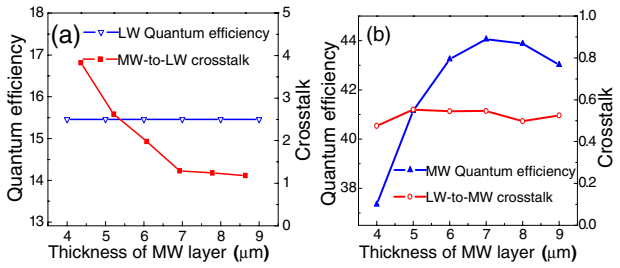

Fig. 2. (a) LW QE and MW-to-LW cross talk and (b) MW QE and LW-to-MW cross talk as a function of the thickness of the MW layer for the infrared detector. The QE is calculated at the cutoff wavelength.

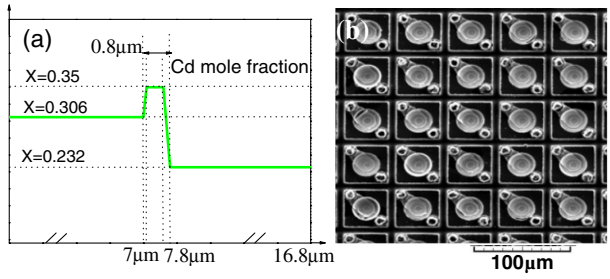

Fig. 4. (a) Designed Cd mole fraction of p1, P, and p2 layers during the HgCdTe material epitaxial growth. (b) SEM image of the 128×128 LW/MW HgCdTe two-color infrared FPA detector.

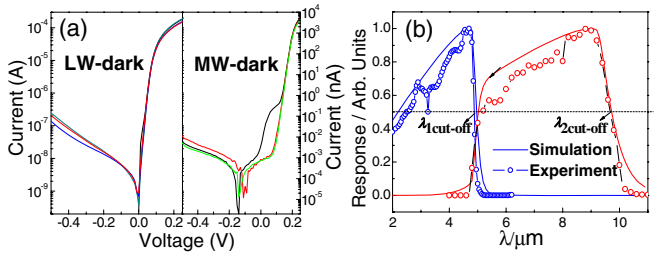

Fig. 5. (a) Dark current characteristics of LW and MW junctions. (b) Experimental (dotted) and simulated (solid) spectral photoresponse of the LW/MW HgCdTe two-color infrared detector with cutoff wavelengths of $\lambda_{1\ \mathrm{cutoff}} = 4.8$ μm and $\lambda_{2\ \mathrm{cutoff}} = 9.7$ μm for the LW and MW diodes, respectively. A voltage of 0.01 V is used in the simulation and experiment.

value due to the grooved structure design, which is used for the n region implantation of the MW photodiode as well as the MW contact. The dark current characteristics of the LW and MW junctions are shown in Fig. 5(a). The average R0A values of MWIR and LWIR are 5.86×10^3 and $30.15\Omega \cdot \mathrm{cm}^2$, respectively. Figure 5(b) shows the spectral photoresponse for the HgCdTe two-color infrared detector with the proposed structure from the previous numerical simulations. The cutoff wavelengths of the LW and MW diode are 4.8 and 9.7 μm, respectively. It can be observed that the cutoff wavelength of the MW diode is close to the turn-on wavelength of the LW diode, in good agreement with the proposed structure and parameters. This effectively enables the MW diode to not only absorb and respond to the MW radiation but also acts as a window for any LW radiation. The simulated spectral photoresponse is also compared to that of experimental results showing that the simulation and experiment are self-consistently in good agreement. The calculated peak detectivity is 3.2×10^{11} and 4.3×10^{10} cm $\mathrm{Hz}^{1/2}$ for the MW and LW photodiodes, respectively. From Eqs. (1) and (2), LW-to-MW cross talk of 1.25% and MW-to-LW cross talk of 0.7% are obtained. Figure 6 is the infrared image from the 128×128 LW/MW HgCdTe two-color infrared FPA detector. It is shown that the proposed grooved two-color HgCdTe infrared FPA detector is very promising for the intelligent identification of infrared objects.

In summary, a 128×128 HgCdTe LW/MW two-color infrared FPA detector is fabricated with the cutoff wavelengths of 4.8 and 9.7 μm, and peak detectivities of 3.2×10^{11} and 4.3×10^{10} cm $\mathrm{Hz}^{1/2}$, respectively. Ultralow LW-to-MW cross talk of 1.25% and MW-to-LW cross talk of 0.7% are obtained showing that the LW/MW two-color HgCdTe infrared FPA detector is very promising for third-generation intelligent infrared imaging.

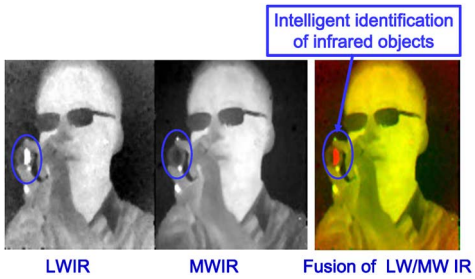

Fig. 6. Infrared image from the 128×128 LW/MW HgCdTe two-color infrared FPA detector at 77 K. A MW optical filter is used to stop MW infrared radiation. The heated electric soldering iron behind the filter is invisible for the MWIR detector (middle) while visible for the LWIR detector (left).

This work was supported in part by the 973 grant of MOST (2013CB632705), NSFC (11322441, 11274331, and 11334008), Fund of Shanghai Science and Technology Foundation (14JC1406400), and the Shanghai Rising-Star Program.

References

1. A. Rogalski, J. Antoszewski, and L. Faraone, J. Appl. Phys. **105**, 091101 (2009).
2. P. Norton, Opto-Electron. Rev. **14**, 1 (2006).
3. J. Schuster and E. Bellotti, Opt. Express **21**, 14712 (2013).
4. W. D. Hu, X. S. Chen, Z. H. Ye, and W. Lu, Appl. Phys. Lett. **99**, 091101 (2011).
5. W. D. Hu, X. S. Chen, Z. H. Ye, Y. G. Chen, F. Yin, B. Zhang, and W. Lu, Appl. Phys. Lett. **101**, 181108 (2012).
6. J. Le Perchec, Y. Desieres, and R. E. de Lamaestre, Appl. Phys. Lett. **94**, 181104 (2009).
7. A. Jozwikowska, K. Jozwikowski, J. Antoszewski, C. A. Musca, T. Nguyen, R. H. Sewell, J. M. Dell, L. Faraone, and Z. Orman, J. Appl. Phys. **98**, 014504 (2005).
8. A. Zemel, I. Lukomsky, and E. Weiss, J. Appl. Phys. **98**, 054504 (2005).
9. W. D. Hu, X. S. Chen, Z. H. Ye, L. Liao, and W. Lu, IEEE J. Sel. Top. Quantum Electron. **19**, 4100107 (2013).
10. A. Rogalski, Rep. Prog. Phys. **68**, 2267 (2005).
11. R. Breiter, T. Ihle, J. C. Wendler, H. Lutz, S. Rutzinger, T. Schallenberg, K. C. Hofmann, and J. Ziegler, Opt. Eng. **50**, 061010 (2011).
12. A. Manissadjian, L. Rubaldo, Y. Rebeil, A. Kerlain, D. Brellier, and L. Mollard, Proc. SPIE **8353**, 835334 (2012).
13. F. Aqariden, J. Elsworth, J. Zhao, C. H. Grein, and S. Sivananthan, J. Electron. Mater. **41**, 2700 (2012).
14. V. Srivastav, R. Pal, R. K. Bhan, V. Dhar, and V. Venkataraman, Infrared Phys. Technol. **61**, 290 (2013).
15. P. Martyniuk, W. Gawron, and A. Rogalski, J. Electron. Mater. **42**, 3309 (2013).
16. P. Ballet, F. Noël, F. Pottier, S. Plissard, J. P. Zanatta, J. Baylet, and O. Gravrand, J. Electron. Mater. **33**, 667 (2004).
17. E. P. G. Smith, L. T. Pham, G. M. Venzor, E. M. Norton, and M. D. Newton, J. Electron. Mater. **33**, 509 (2004).
18. E. P. G. Smith, E. A. Patten, P. M. Goetz, G. M. Venzor, J. A. Roth, and B. Z. Nosho, J. Electron. Mater. **35**, 1145 (2006).
19. E. P. G. Smith, G. M. Venzor, A. M. Gallagher, M. Reddy, J. M. Peterson, D. D. Lofgreen, and J. E. Randolph, J. Electron. Mater. **40**, 1630 (2011).
20. Z. Ye, W. Zhou, W. Hu, X. Hu, R. Ding, and L. He, J. Infrared Millim. Waves **28**, 4 (2009).
21. W. D. Hu, X. S. Chen, Z. H. Ye, and W. Lu, Semicond. Sci. Technol. **25**, 045028 (2010).
22. K. Jozwikowski and A. Rogalski, J. Appl. Phys. **90**, 1286 (2001).
23. J. Wenus, J. Rutkowski, and A. Rogalski, IEEE Trans. Electron Devices **48**, 1326 (2001).
24. E. Bellotti and D. D. Orsogna, IEEE J. Quantum Electron. **42**, 418 (2006).
25. J. G. A. Wehner, E. P. G. Smith, W. Radford, and C. L. Mears, J. Electron. Mater. **41**, 2925 (2012).
26. Sentaurus Device User Guide, Version G-2012.06 (Synopsys, 2012).
27. H. Kocer, Y. Arslan, and C. Besikci, Infrared Phys. Technol. **55**, 49 (2012).